Supporting Information

Multi-Functional Nitrile-Based Electrolyte Additives Enable Stable Lithium Metal Batteries with High-Voltage Nickel-rich Cathode

Shu Yang[a†], Haonan Huang[b†], Hailin Shen[c], Mengyuan Zhou[a], Liang Yuan[a], Yunyun Gao[a], Jinlei Zhang[a], Yike Wei[a], Changchun Ye[b,d*], Weishan Li[b], Zhenghui Pan[a*]

[a] School of Materials Science and Engineering, Tongji University, Shanghai 201804, China

[b] School of Chemistry, South China Normal University, Guangzhou 510006

[c] School of Chemical Engineering and Materials, Changzhou Institute of Technology, Changzhou, China

[d] School of Physics and Optoelectronics, South China University of Technology, Guangzhou 510006, China

[†] S.Yang and H. Huang contributed equally to this work.

*Corresponding Author E-mail: zhenghuipan@tongji.edu.cn; esyecc@mail.scut.edu.cn
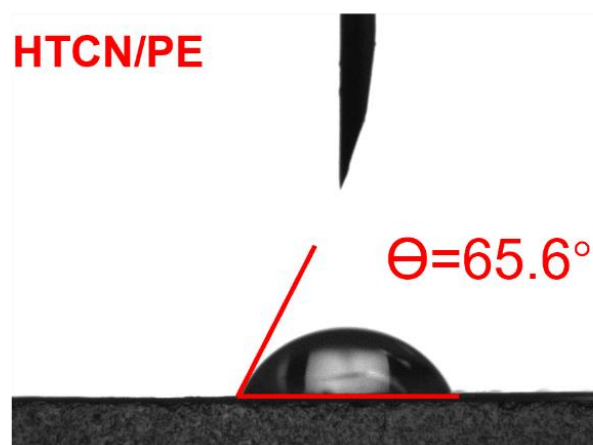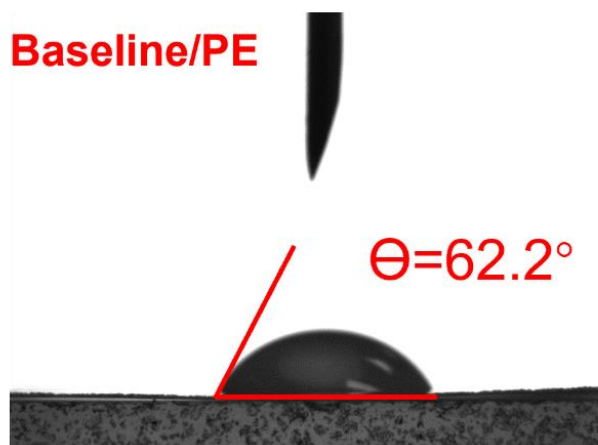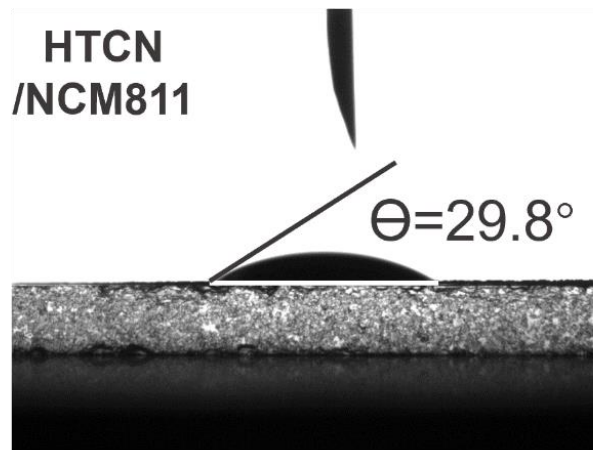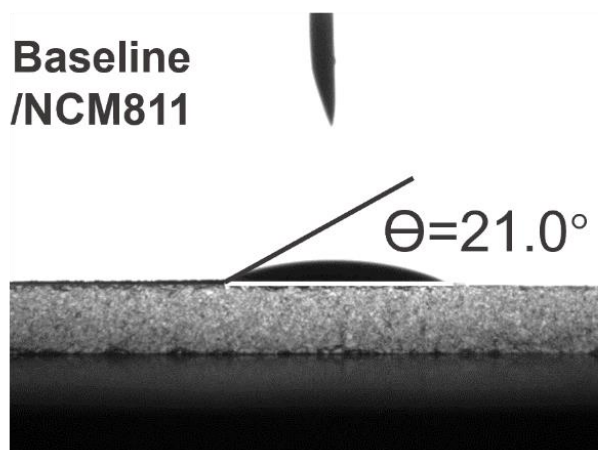
Fig. S1 The contact angle between NCM811 electrodes and electrolytes without or with additives.
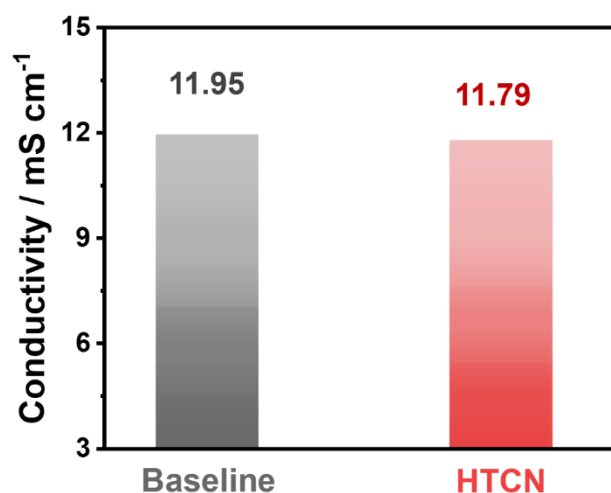
Fig. S2 Ionic conductivity of baseline, 0.5% DTD-, 0.5% HTCN- and DTD+HTCN-containing electrolytes, measured at room temperature.

The physical properties of electrolytes may affect the electrochemical behaviour of batteries. It can be found that the contact angle between the NCM811 electrode and electrolyte increases from 21.0º to 29.8º with the use of the HTCN additive (**Fig. S1**). At the same time, the ionic conductivity of electrolytes decreases from 11.95 to 11.79 mS cm^{-1} (**Fig. S2**), suggesting that the effect of HTCN additive on the cyclic stability and discharge capacity is related to their impact on the interfacial property rather than physical properties of electrolytes.
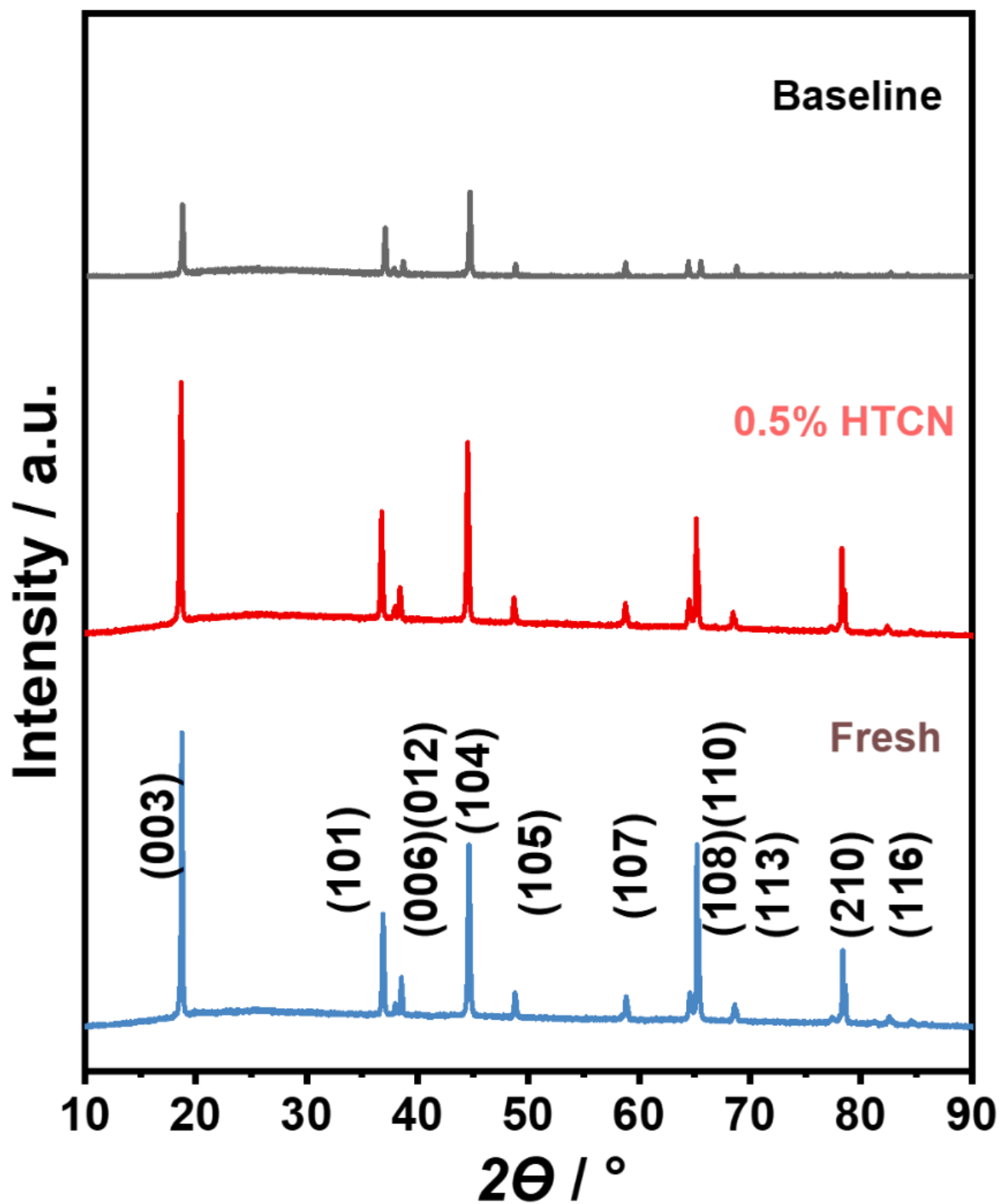
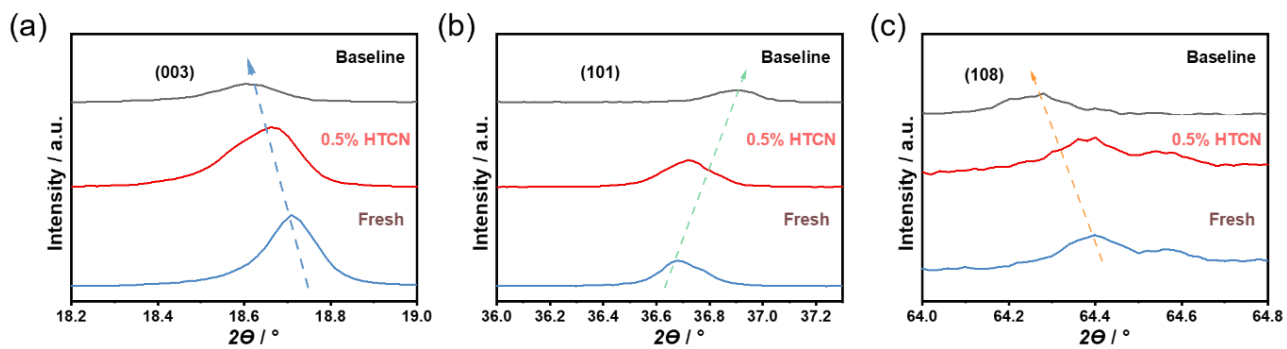**Fig. S3** XRD patterns of NCM811 electrodes after 150 cycles in various electrolytes.

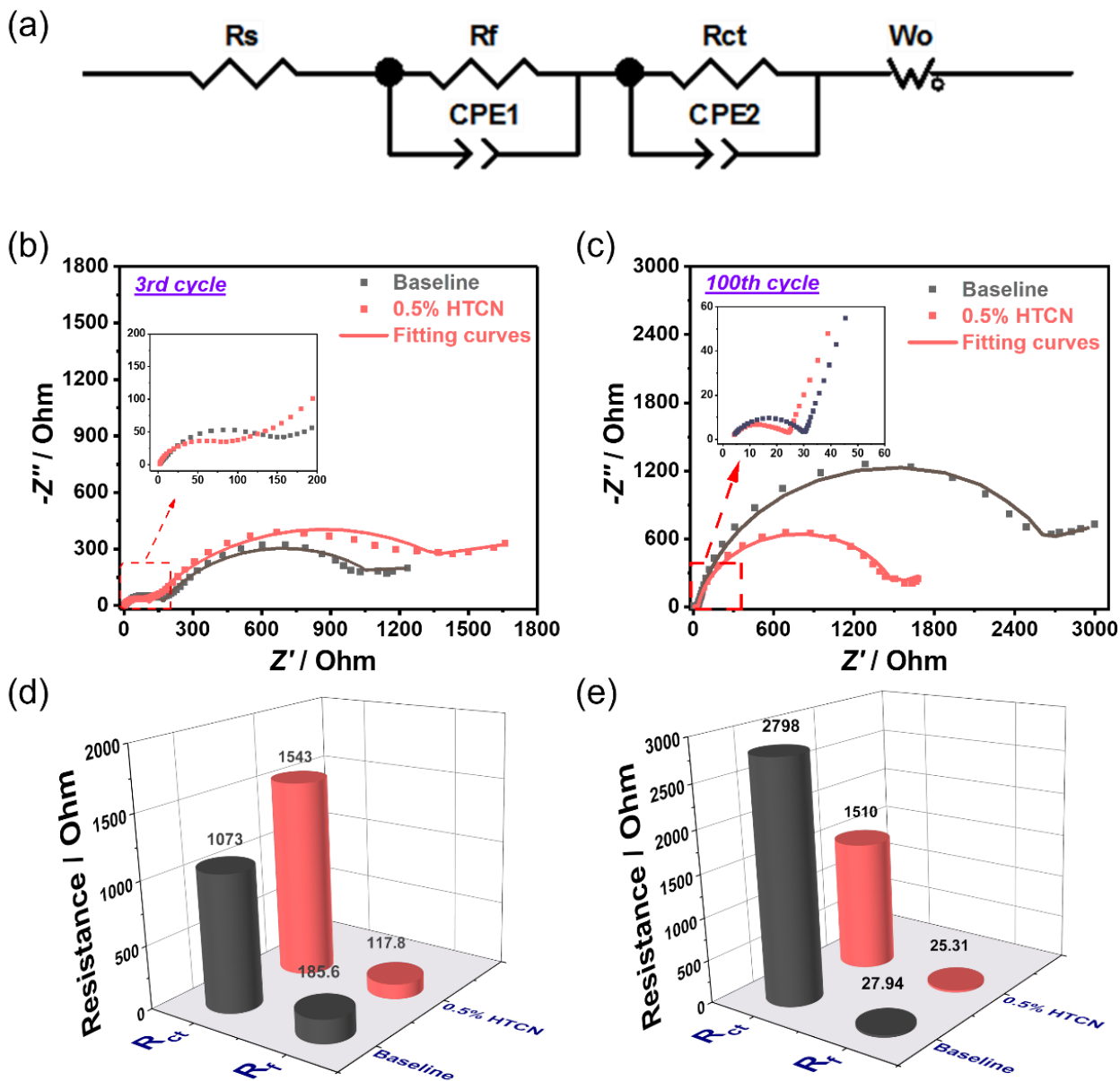**Fig. S4** XRD patterns of NCM811 electrodes after 150 cycles in various electrolytes.

Fig. S5 (a) Equivalent circuit for fitting the EIS plots; Nyquist plots of L-NCM811/Li half-cells at the (b) 3rd and (c) 100th cycle in various electrolytes; (d, e) Obtained value of R_f and R_{ct} by fitting the EIS plots using the equivalent circuit.
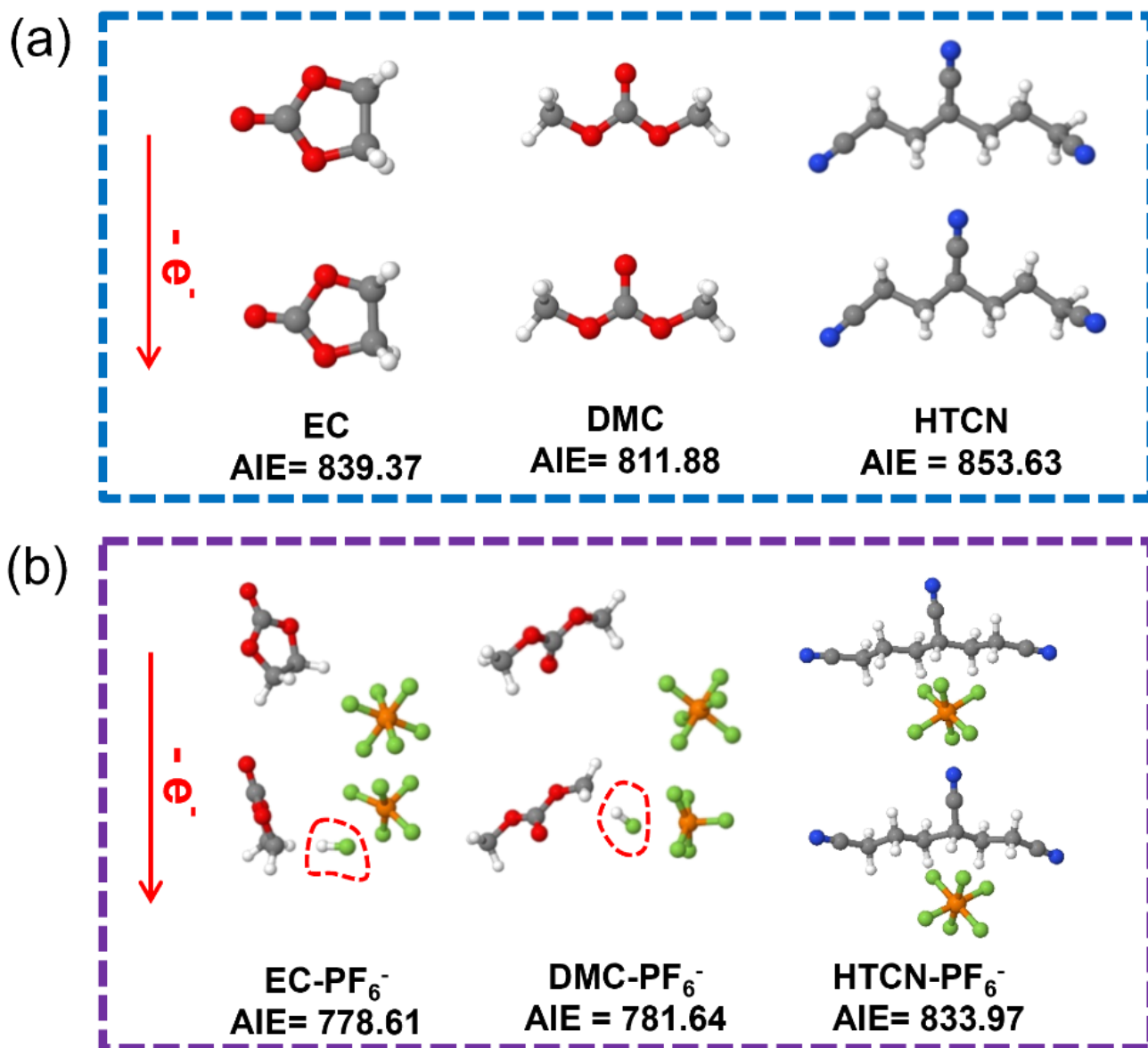
Fig. S6 Optimized structures and corresponding adiabatic ionization energies (AIE, kJ mol^{-1}) of EC, DMC, HTCN and their clusters with PF$_6^-$ anion.
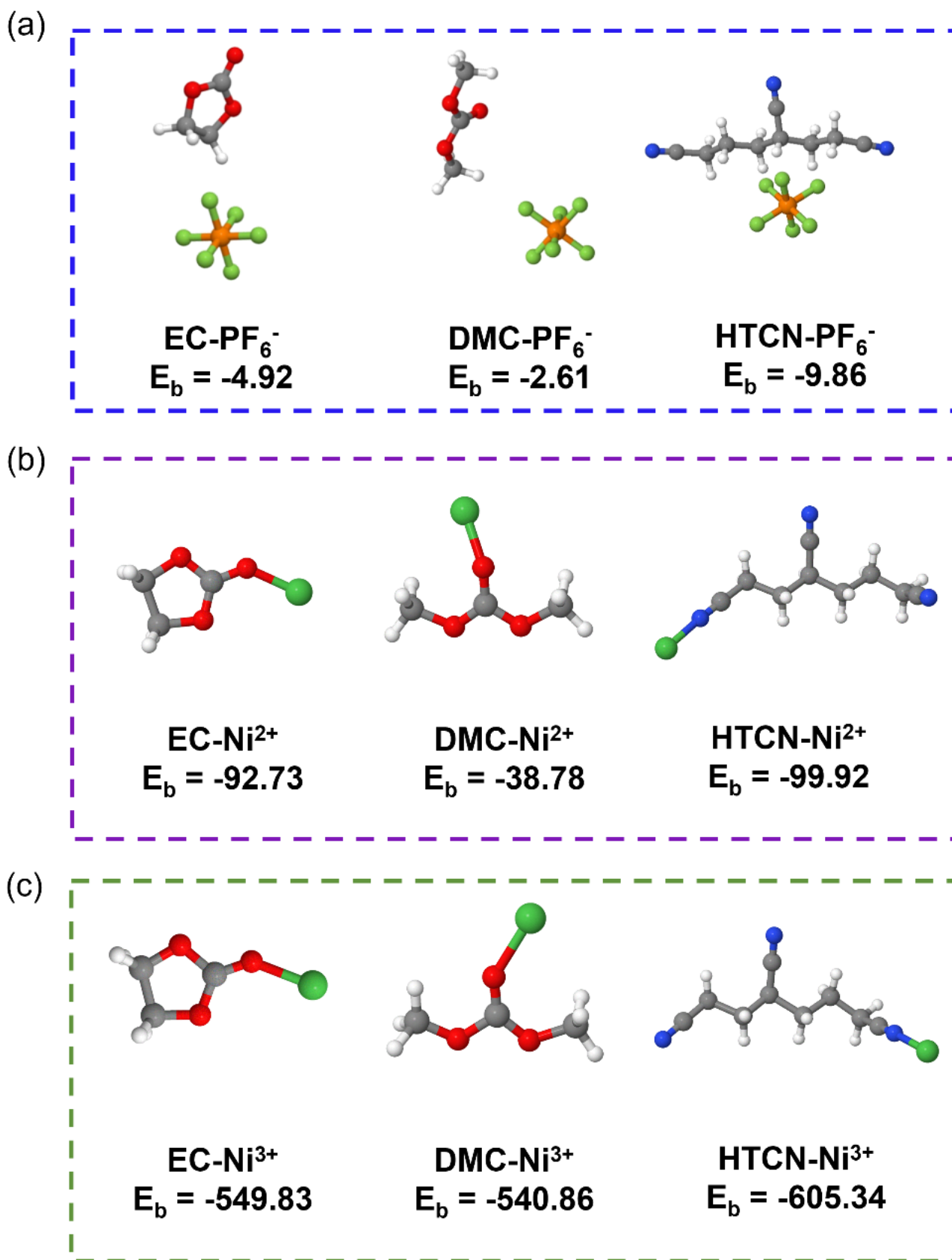
Fig. S7 Optimized structures and calculated binding energy (kJ mol^{-1}) between (a) PF_6^-, (b) Ni^{2+} and (c) Ni^{3+} ion with HTCN additive or electrolyte solvents.
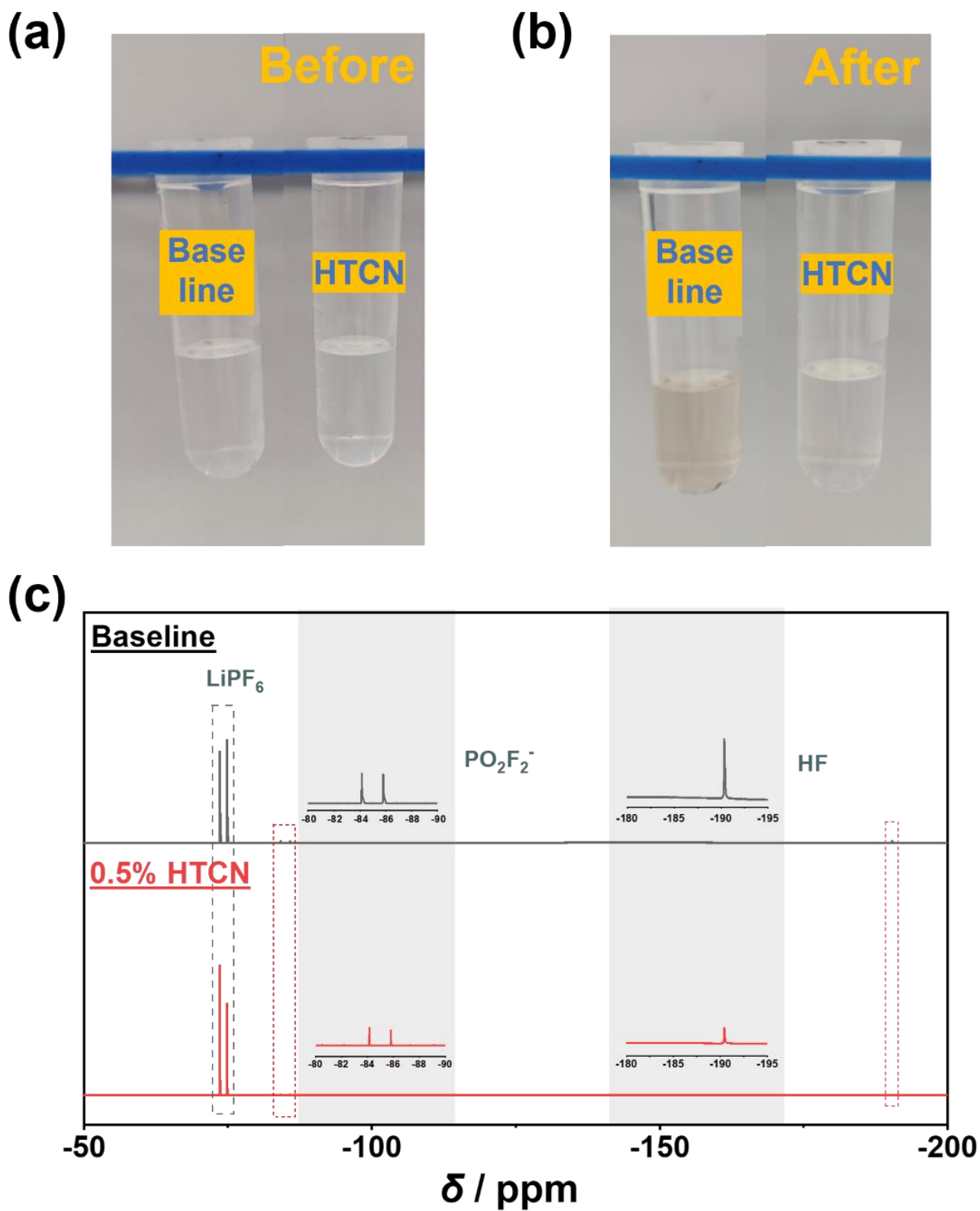
Fig. S8 Color change of (a) baseline and (b) HTCN-containing electrolytes after storage at 55 °C for 3 days. (c) ^{19}F NMR spectra of baseline and HTCN-containing electrolytes after storage at 55 °C for 3 days.

Lithium-ion batteries containing $LiPF_6$-based electrolytes have poor stability, resulting in the thermal decomposition and hydrolysis of PF_6^-, followed by the generation of hydrofluoric acid (HF). As exhibited in Fig. S8, after storage at 55 °C for 3 days, HTCN-containing electrolyte shows less presence of $PO_2F_2^-$ and HF in comparison to baseline electrolyte, manifesting that the adding of HTCN enhances the stability of electrolyte due to the firm combination between HTCN and PF_6^- ion.
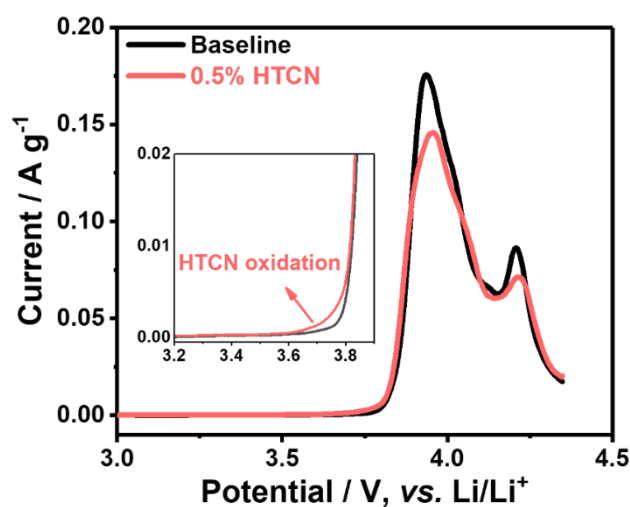

Fig. S9 LSV curves of various electrolytes on NCM811 electrode in L-NCM811(1:1:1)//Li coin cells from OCP to 4.35 V at a scan rate of 0.1 mV s^{-1}, in which the ratio of NCM811: PVDF: AB is 1:1:1.
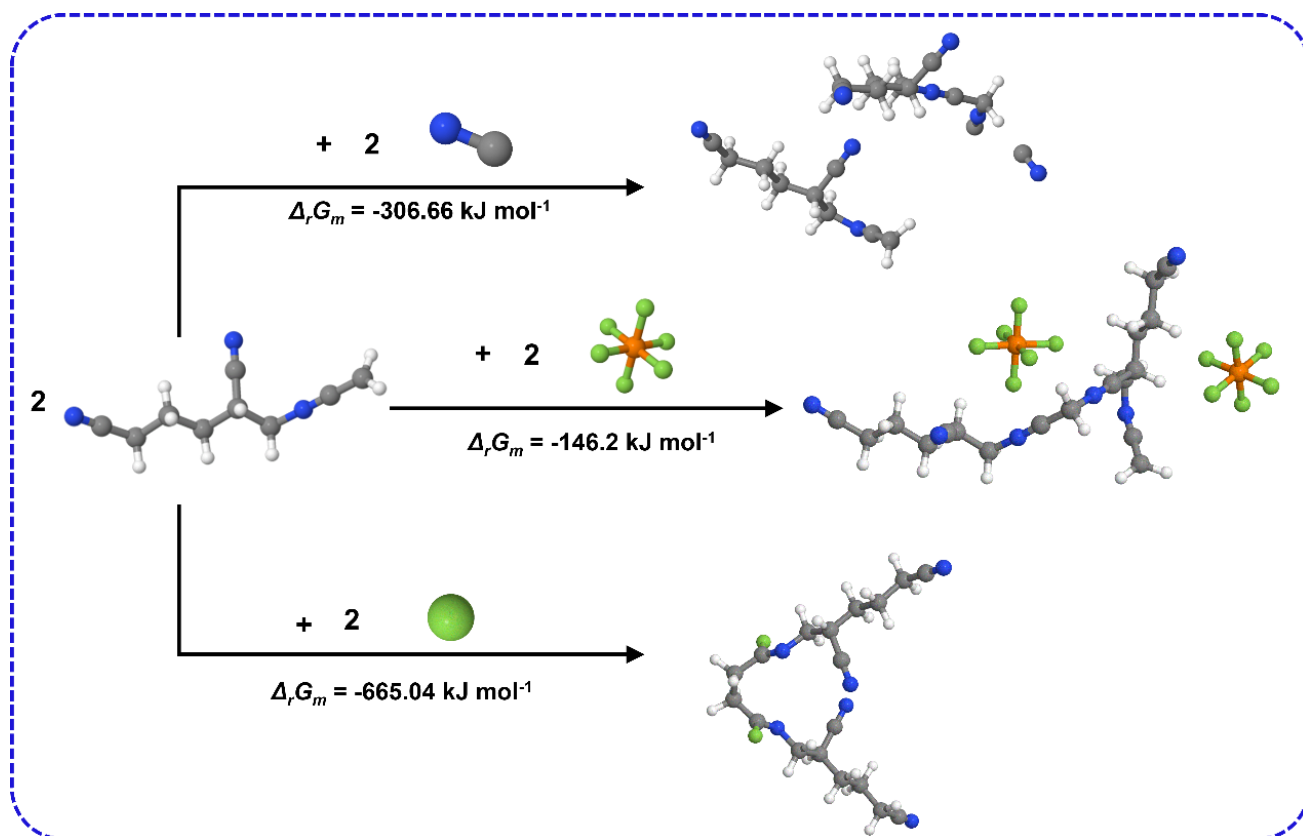
Fig. S10 The possible oxidation paths of HTCN together with their corresponding free energy change.
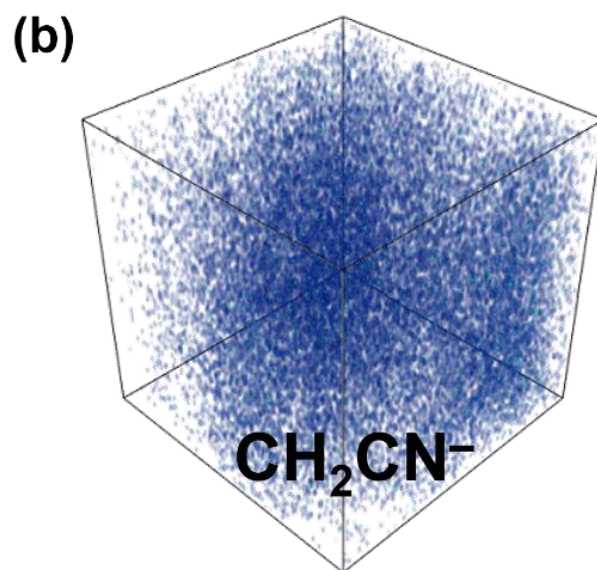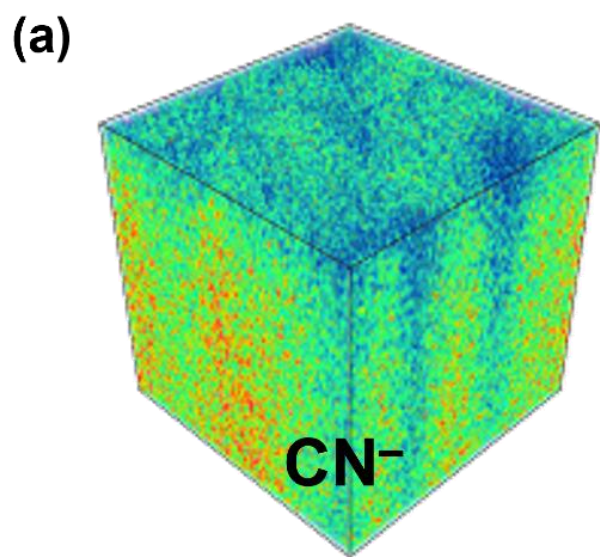
Fig. S11 Corresponding 3D reconstruction distribution mappings of CN^- and CH_2CN^- species on NCM811 surface after cycling in HTCN-containing electrolytes measured by TOF−SIMS.
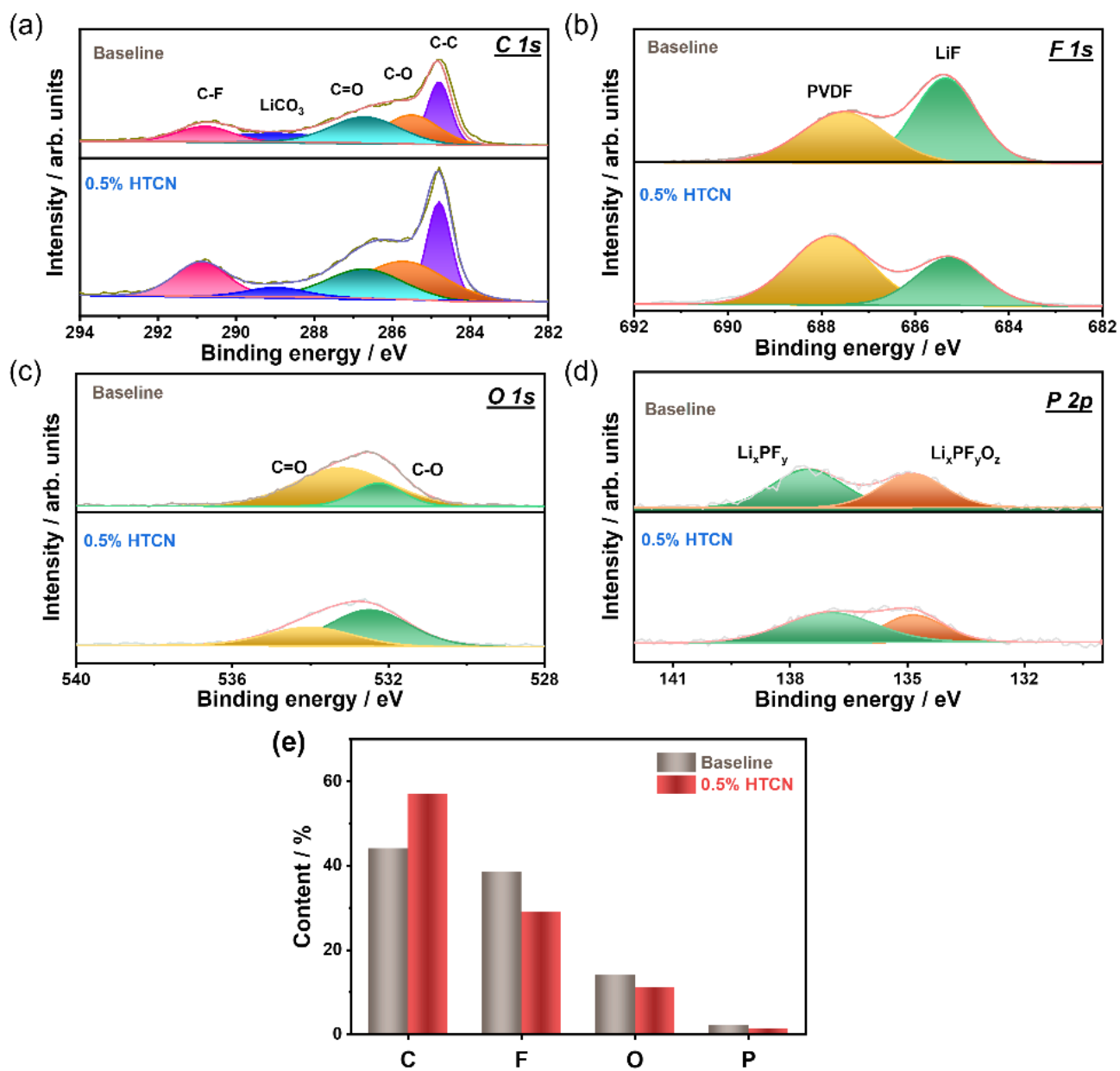
Fig. S12 XPS spectra of NCM811 electrodes retrieved from L-NCM811/Li cells after 20 cycles in baseline and additive-containing electrolytes: (a) O 1s, (b) F 1s, (c) P 2p and (d) O 1s; (e) Obtained contents of various elements on the L-NCM811 electrodes after 20 cycles.
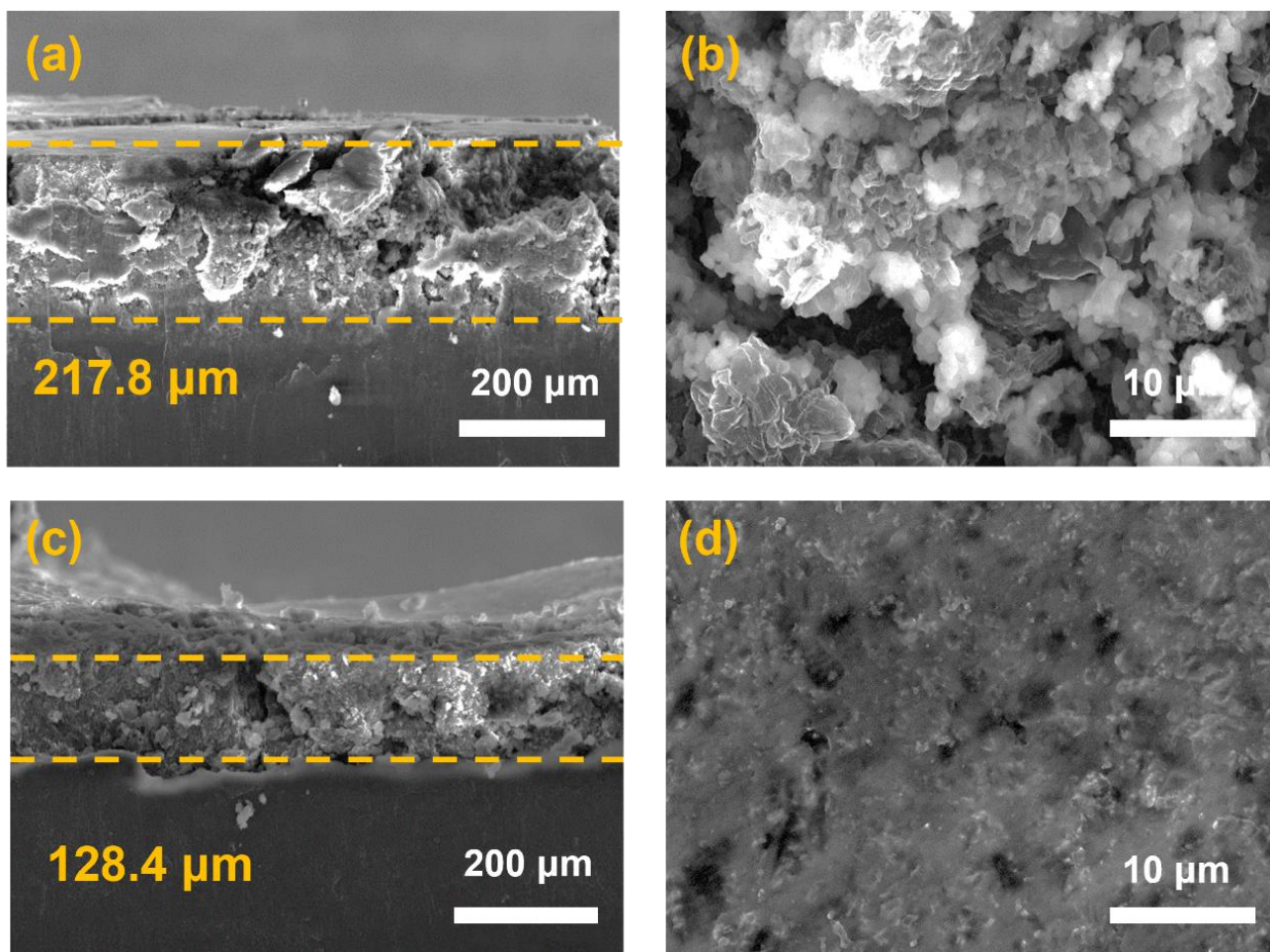
Fig. S13 Cross-sectional and top-view SEM images of the Li electrode recovered from the Li/Li cells after 300 h in (a, b) baseline and (c, d) HTCN-containing electrolytes.
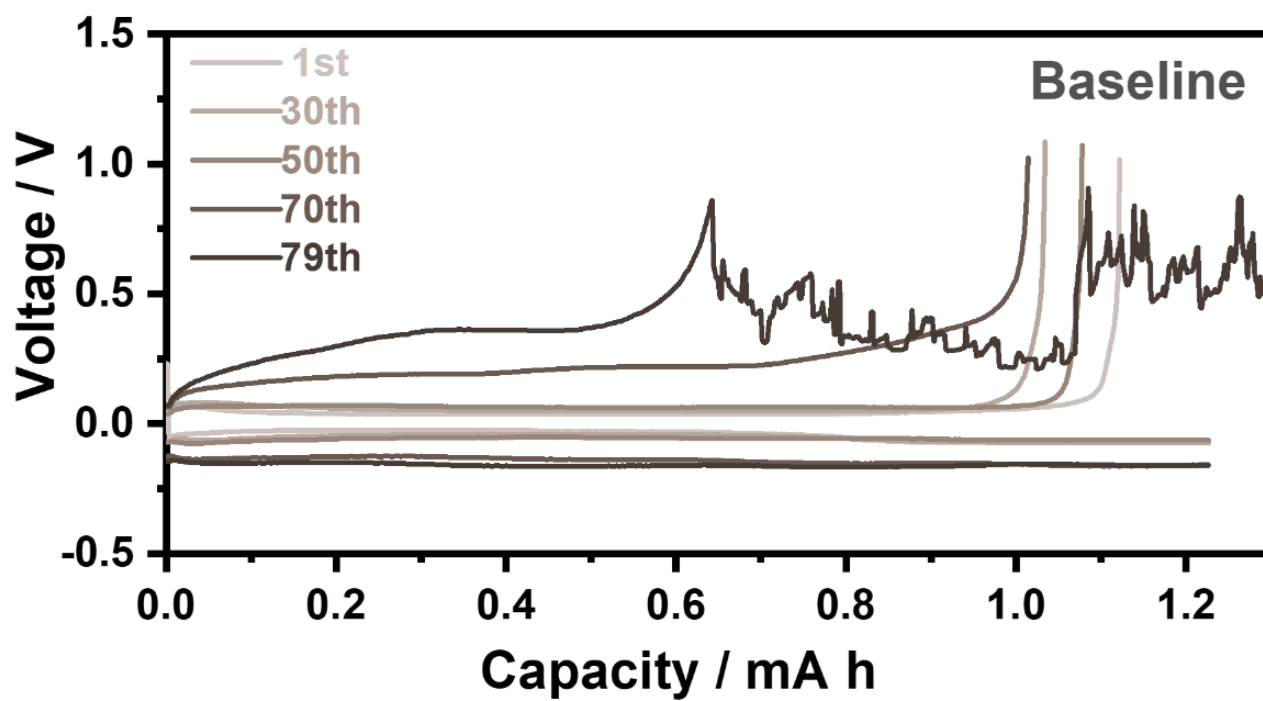
Fig. S14 Select plating/stripping curves of Li/Cu cells in baseline electrolyte.
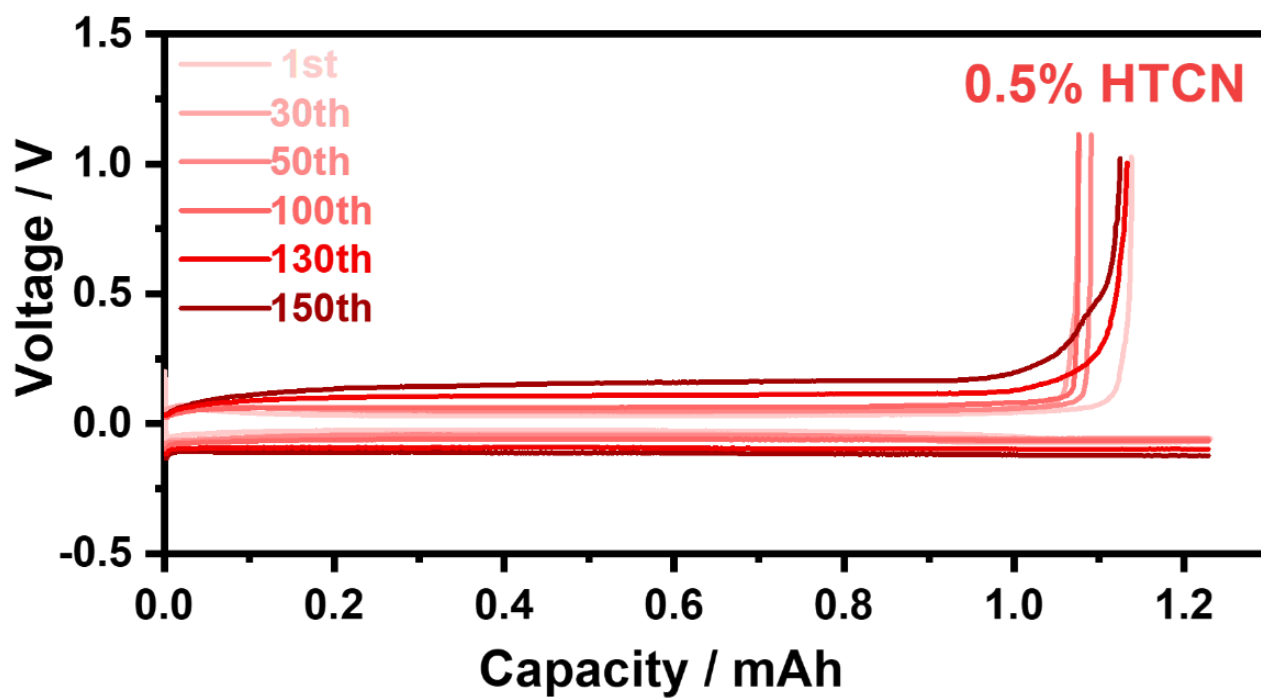
Fig. S15 Select plating/stripping curves of Li/Cu cells in HTCN-containing electrolyte.
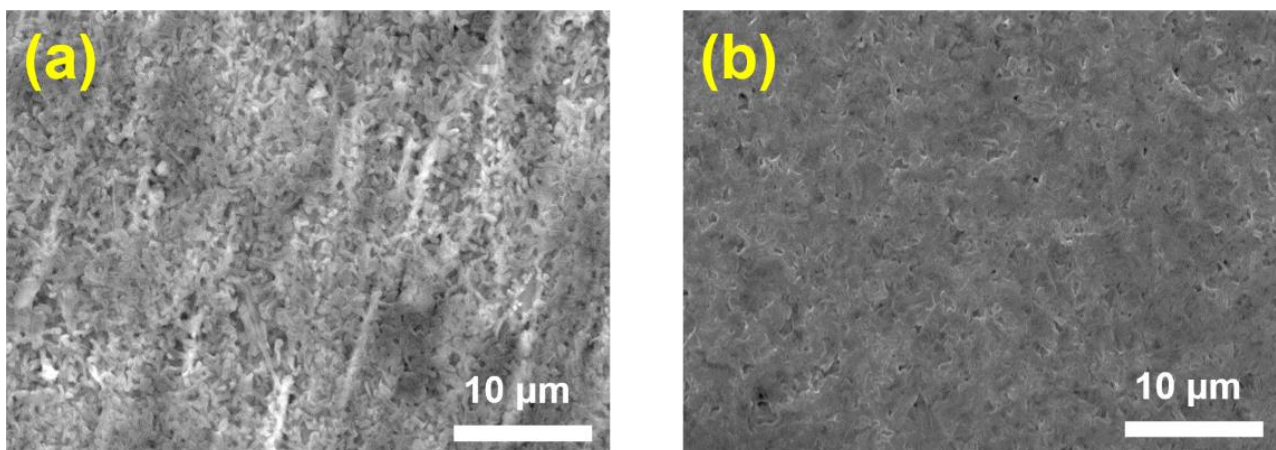
Fig. S16 Top–view images of deposited Li on Cu electrodes in (a) baseline and (b) 0.5% DTD-, (c) 0.5% HTCN- and (d) DTD+HTCN-containing electrolytes at 1 mA cm^{-2} for 0.5 h.
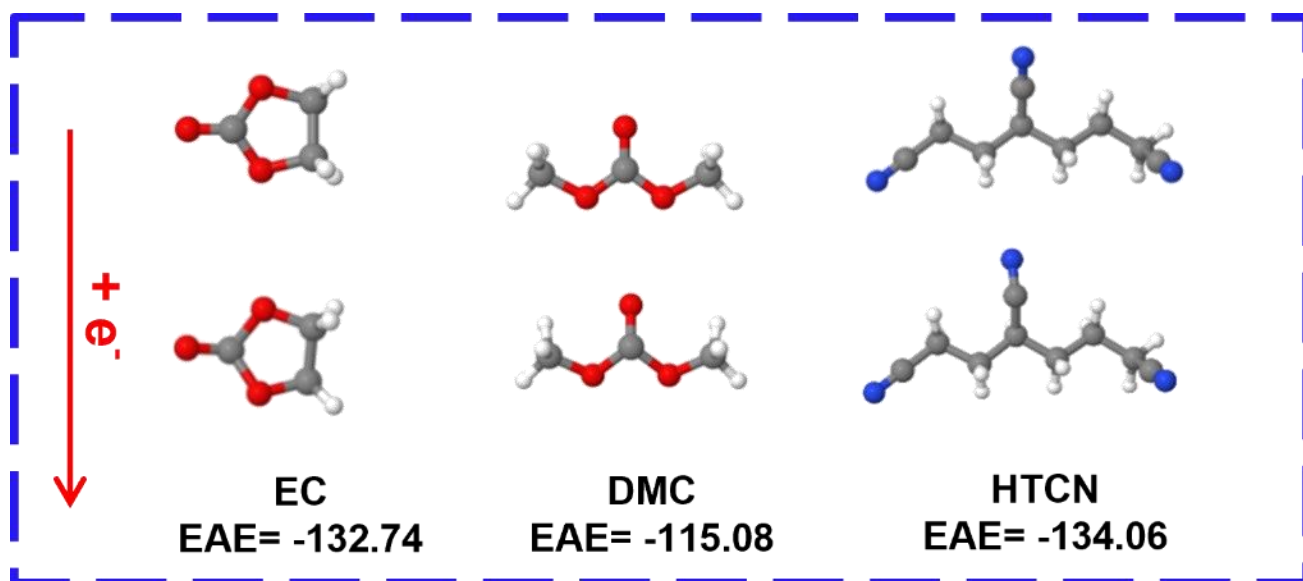
Fig. S17 Optimized structures and corresponding electronic affinity energy (EAE, kJ mol^{-1}) of EC, DMC and HTCN.
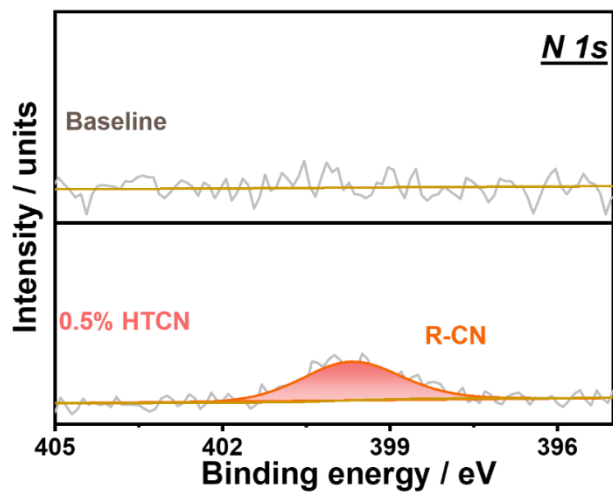
Fig. S18 N 1s XPS spectra of Li electrode recovered from Li/Li cells after 20 cycles in HTCN additive-containing electrolyte
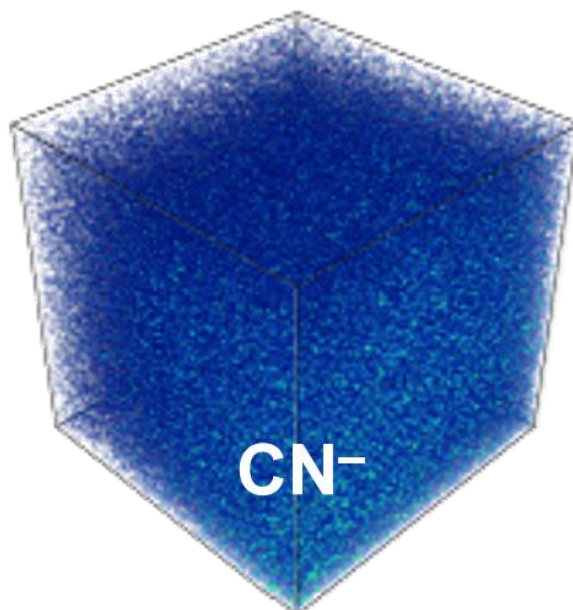
Fig. S19 3D reconstruction distribution mappings of CN⁻ on the surface of Li metal anode after cycling in HTCN-containing electrolyte measured by TOF−SIMS.
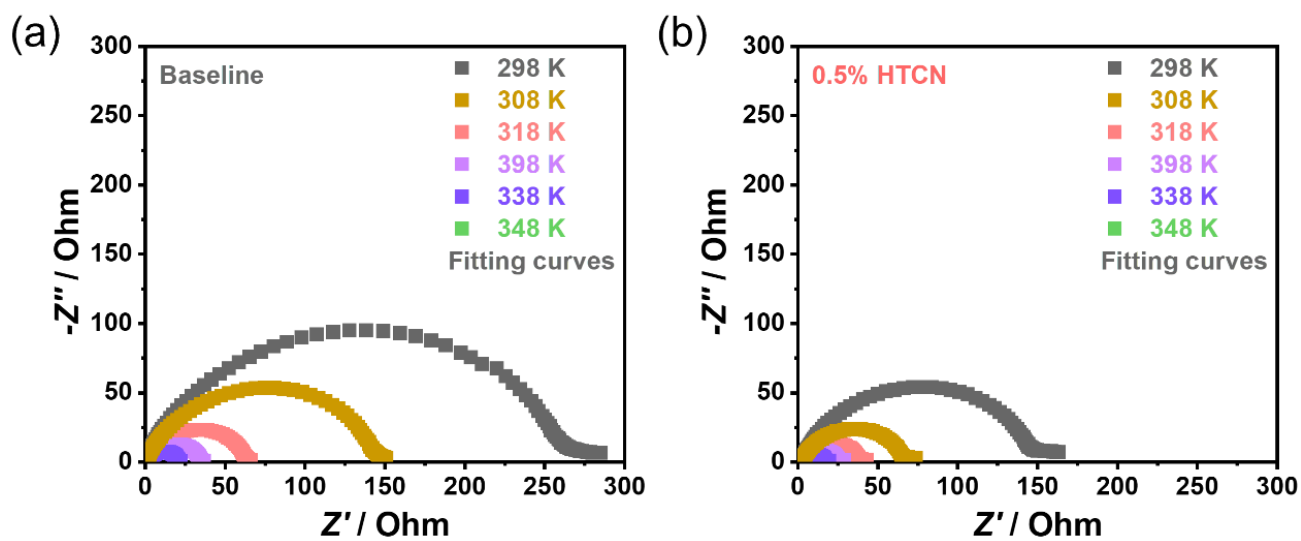
Fig. S20 Temperature-dependent EIS plots of Li symmetric cells in baseline and HTCN-containing electrolytes.
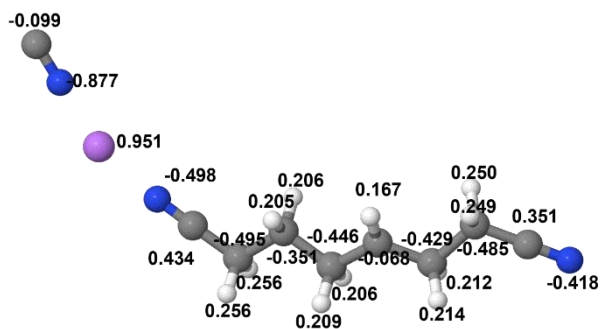

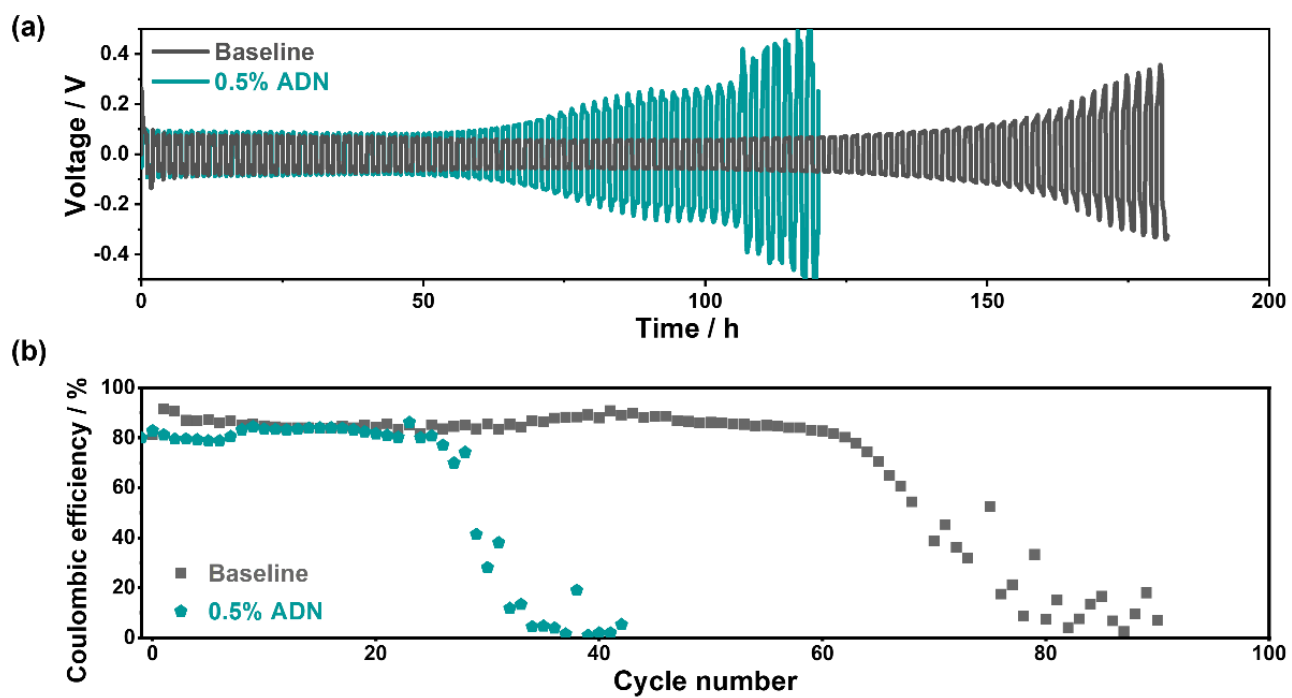**Fig. S21** NBO charge distribution of M-[Li$^+$(HTCN)]$^{\bullet-}$.

Fig. S22 (a) Cyclic stability of Li//Li symmetric cells and (b) CE of Li//Cu asymmetric cells in baseline and ADN-containing electrolytes.
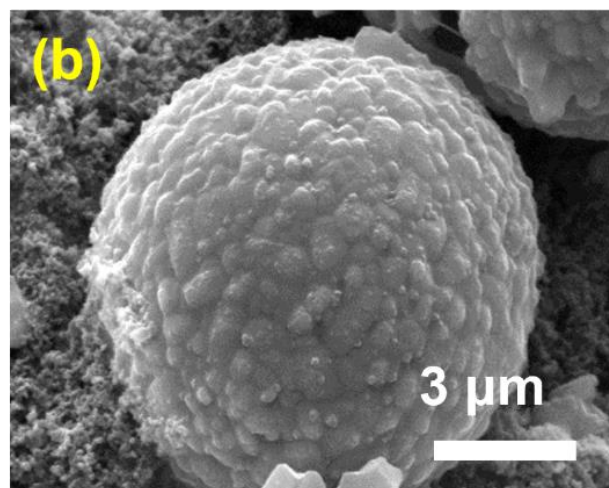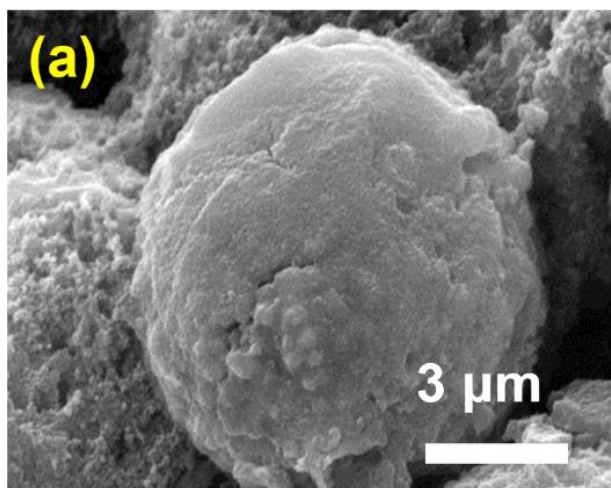
Fig. S23 SEM images of H-NCM811 cathode recovered from H-NCM811//Li full batteries after 100 cycles in (a) baseline and HTCN-containing electrolytes.
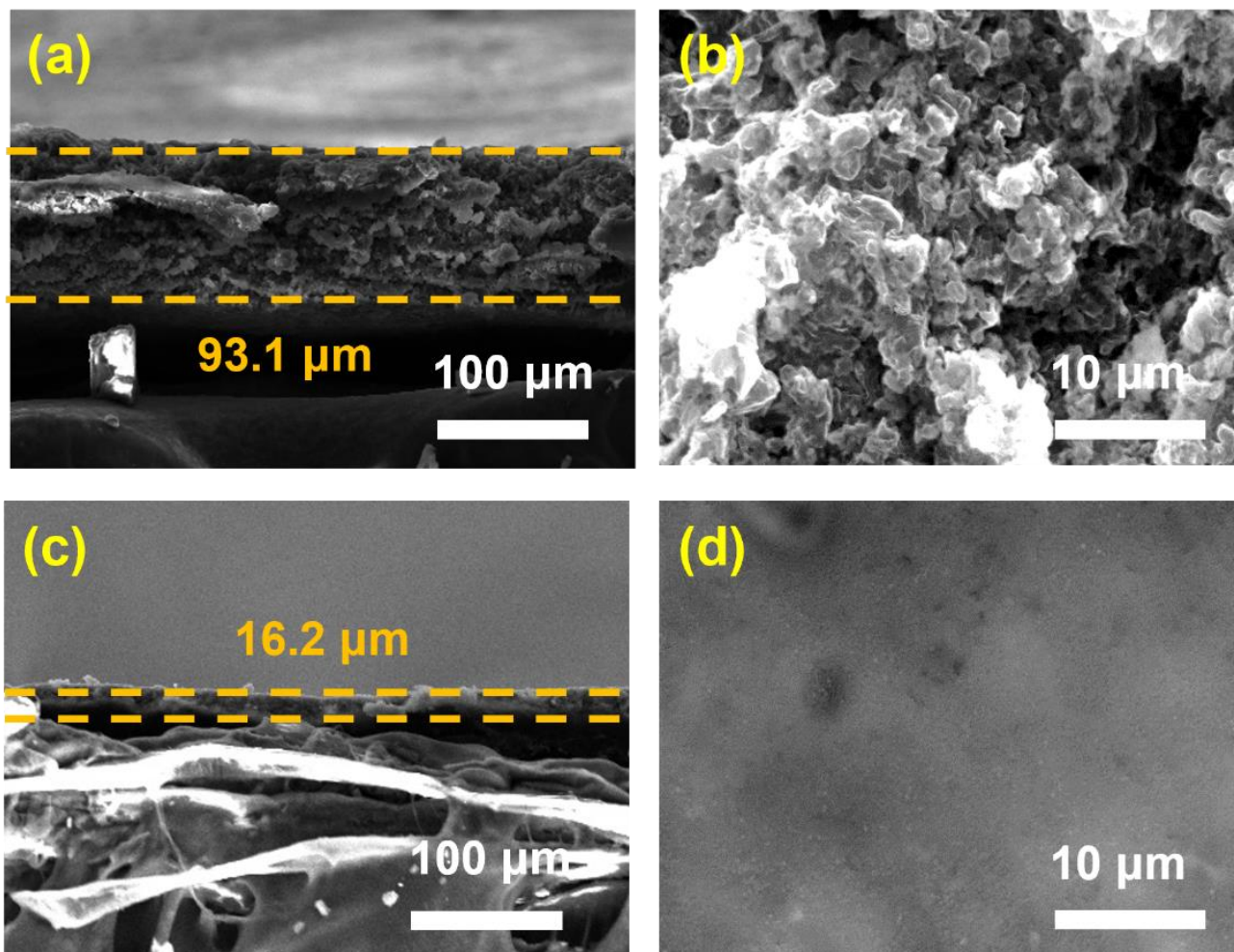
Fig. S24 Cross-sectional and top-view SEM images of the Li anode recovered from H-NCM811/Li full batteries after 200 h in (a, b) baseline and (c, d) HTCN-containing electrolytes.